



Effects of Wing Tip Shaping on Noise Generation

Christine E. KLEI¹; Rainer M. BUFFO²; Eike STUMPF³

Institute of Aerospace Systems, RWTH Aachen University, Germany

ABSTRACT

Geometrical shaping of wing tips leads to variations in the axial and tangential velocity components of the developing vortex. This effect is taken as basis for further analyses of a generic wing model with exchangeable tips in a wind tunnel. Flow field measurements using 3C-PIV and acoustic measurements are performed in order to indicate how changes of the wing tip shape affect noise generation caused by different flow development. High-resolution flow field measurements allow for detailed analyses of the vortex structure and distribution around the wing tip region. Furthermore, beamforming methods are used in order to localize the noise source and show the overall noise reduction potential of different wing tip shapes. The combination of PIV and acoustic measurements allows for a better understanding of underlying physical effects and correlations. Analyses of the data prove a variation of both, flow field and noise characteristics, dependent on the geometrical shape of the wing tip.

Keywords: aeroacoustics, wing tip vortex, geometrical shaping.

I-INCE Classification of Subjects Number: 21.6

NOMENCLATURE

α	angle of attack, °
ω	vorticity, $1/s$
Γ	circulation, m^2/s
σ	standard deviation
b	span, m
c	chord length, m
f	frequency, Hz
r	radius, m
s	halfspan, m
t	thickness, m
u, v, w	velocity components along x, y, z , m/s
x, y, z	Cartesian coordinates, m
AR	aspect ratio
Re	Reynolds number

S	area, m^2
St	Strouhal number
U	freestream velocity, m/s
V	velocity, m/s

SUBSCRIPTS

a	axial
c	chord
r	radial
ref	projection
std	standard deviation
t	tangential
x, y, z	coordinate's direction
TE	trailing edge
∞	freestream condition

1. INTRODUCTION AND MOTIVATION

With growing air traffic in the coming years, noise exposure particularly in the vicinity of airports will increase substantially. In order to remedy such tendencies, approaches to reduce the noise emitted by aircraft need to be enhanced significantly. Especially during approach, where flow-induced noise holds a relevant share of total noise emission, a decrease of aerodynamic noise sources on high lift

¹ klei@ilr.rwth-aachen.de

² buffo@ilr.rwth-aachen.de

³ stumpf@ilr.rwth-aachen.de

devices as well as the wing tip can show a significant effect. In the medium term, the increasing noise annoyance caused by air traffic may lead to more strict regulations and possibly to further capacity constraints. Already today many airports are capacity constrained due to the wake vortex separation distances. These are imposed because of the high concentration of aircraft at low altitude in the circumference of airports where wake vortex encounter is most riskful.

For the design of new aircraft, vortex mitigation and noise reduction methods become increasingly important. If noise reduction is simultaneously accompanied by a more favorable vortex structure regarding strength and stability, compliance with noise restrictions can be met alongside diminishment of the minimum distance during take-off and landing.

Form preparatory research at the Institute of Aerospace Systems (ILR) of RWTH Aachen University it became evident, that for given lift values the geometrical shape of the wing tip greatly influences the vortex structure. Since noise in the wing tip region develops according to aerodynamic conditions, variation of the wing tip shape will influence the aeroacoustic characteristics as well. However, very few investigations of these phenomena are found in literature, lacking systematic analyses. They are still posing significant questions concerning the physical understanding of the linkage between sound radiation and geometrical shaping of wing tips. Studies focusing on noise mechanisms of airfoils predominantly only consider symmetrical airfoils (i.a. 3, 5, 11, 14), often use airfoils with infinite span (1, 5, 7), thus not considering effects at the wing tip, and focus on rather low Reynolds numbers (2, 7, 8, 14). Investigations using models with slats (8) and flaps (13, 15) are not considered for comparison as an additional vortex system is inserted and hence flow structures show a different behavior. Brooks and Marcolini (4) analyze noise prediction models using their experimental data, but they do not show a correlation to flow field data or vortex structure and do not include geometrical shaping.

Buffo et al. (4) investigated vortex structures caused by different wing tip geometries in water tunnel experiments using a Clark-Y profile of aspect ratio $AR = 5$, equal to this study. Results of their measurements for two different wing tip shapes, which are similar to those investigated in this study, are shown in Figure 1. It is clearly visible, that the developing vortices differ in formation, shape, and merging depending on the geometry. As an example, it can be seen that the merging of primary and secondary vortices occurs within the first eighth of the chord length downstream of the trailing edge for a rectangular wing with rounded side edge, Figure 1 left, while vortex cores for an elliptically shaped tip (equivalent to the layout "080x080" as described below) are still separated at equal distance to the trailing edge, Figure 1 right. Taking this as basis, wind tunnel experiments complement the analysis of flow structures by adding investigations of noise generation.

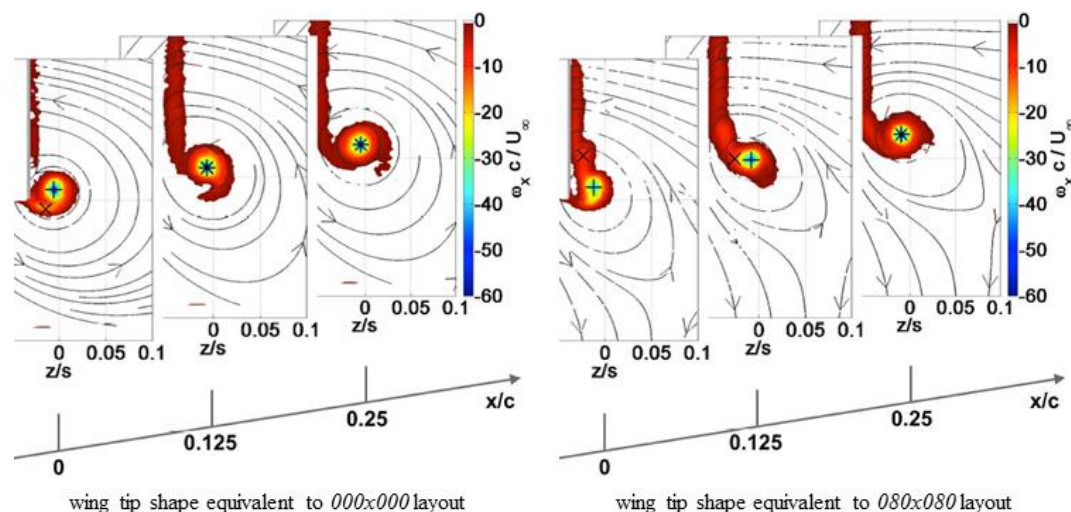


Figure 1 – Vorticity contours downstream of different wing tip models according to Buffo et al. (4).

2. WING MODEL AND TIP GEOMETRIES

During experiments in the wind tunnel at ILR a generic half wing model characterized by exchangeable tip parts is used. Different planform shapes of wing tips are investigated under various angles of attack as well as different flow velocities. For each configuration and setup flow field

measurements using stereoscopic particle image velocimetry (3C-PIV) as well as acoustic measurements using a microphone array are conducted.

As wing model an unswept wing with Clark-Y profile of 320 mm chord length is used to which different wing tips can be attached. Those are designed in a way to keep the aspect ratio $AR = b^2/S_{ref}$ constant at $AR = 5$, thus leading to a halfspan $s = b/2$ of about 800 mm length, dependent on the projected area S_{ref} of the tip geometry. The lateral edge is rounded for all cases presented.

Denotations of the tip models are defined by their geometrical shape, consisting of the starting points of the quarter-ellipse (see Figure 2 a): Reference wing tip *000x000* is based on a rectangular wing without elliptical shaping at the tip, thus only the side edge is rounded (Figure 2 b, left). Introducing a quadrant at the leading edge up to one fourth of the chord length (80 mm) in spanwise and chordwise direction tip *080x080* is formed (Figure 2 b, center). Extending the chordwise stretch of the elliptical shape to the trailing edge characterizes the third tip model, *080x320*, keeping the spanwise starting point at the same position as before (Figure 2 b, right). Tip parts are attached to the main wing body of 600 mm span. When mounting the model in the wind tunnel, a split plate is used to avoid boundary layer influences of the support structure.

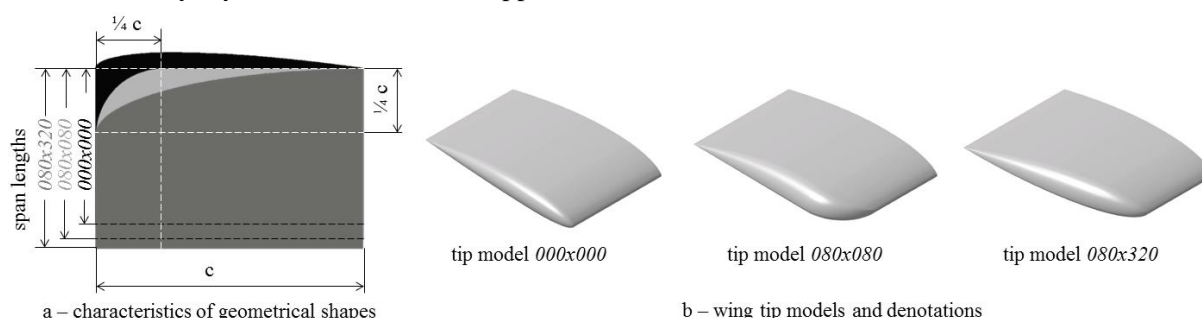


Figure 2 – Geometric shapes of wing tip models.

3. MEASUREMENT EQUIPMENT AND EXPERIMENTAL SETUP OPTIMIZATION

Measurements have been carried out in a closed circuit, ‘Goettingen’ type wind tunnel with open test section of 3 m in length and a 1.5 m diameter of the nozzle. The contraction ratio of the nozzle is 1:4.84 with the maximum obtainable speed amounting to $U_\infty = 75$ m/s.

The measurement coordinate system is defined in a way that the x -axis points in free stream direction, the y -axis along the wing span, and the z -axis orthogonal forming a right-handed system with the origin located at the vortex center.

3.1 Acoustic measurement equipment

In order to perform acoustic measurements, an array of clustered microphones is installed in the wind tunnel as shown in Figure 3 a. Length and height of the array are 1 m each. The acquisition device limits the maximum number of microphones to 32. As a result of former analyses an optimized setup was found, placing 30 microphones arbitrarily along the outer section of the array and two microphones near the center. The array is mounted at a distance between 1630 and 1650 mm to the wing’s trailing edge, depending on the angle of attack.

$\frac{1}{2}$ ” Sennheiser KE 4-211-2 microphones with flat frequency response for the range between 20 Hz and 20 kHz are used. Calibration factors are determined individually by the use of a reference speaker.

3.2 Flow field measurement equipment

In order to perform particle image velocimetry, a system of cameras, laser, and optical devices is installed. *DEHS* is chosen as suitable seeding since it meets the requirements of particle size, density, and light scattering as well as flow following behaviors. The seeding generator is placed immediately downstream of the measurement section. Two separately controllable, frequency-doubled *Nd-YAG*-lasers, generating light of a wavelength of 532 nm, are used as light sources, the energy of the light pulses being 120 mJ each. They are mounted on a traversing system as several planes perpendicular to flow direction are investigated. The light sheet is installed perpendicular to the flow direction using optical lenses and apertures as well as a mirror. Two digital *CCD* cameras with a resolution of 1376 x 1024 pixels, installed on adapters able to fulfil the Scheimpflug criterion (9), are

used to record the particle images. As optical devices for the cameras, lenses of 50 mm focal length were used, providing the region of interest in high resolution, accounting to a core diameter of the vortex of about 15 pixel.

A stereoscopic setup is chosen, positioning both cameras on the suction side of the model in order to avoid blockage in the field of view due to the model. For calibration of the PIV system and setup a double sided, non-displaced target is used which is moved on coplanar planes of equal distance along freestream direction (12). A sketch of the experimental setup of laser, cameras, and model and target in the wind tunnel can be found in Figure 3 b. All moveable and displaceable parts during measurement series are marked by two arrows indicating the direction.

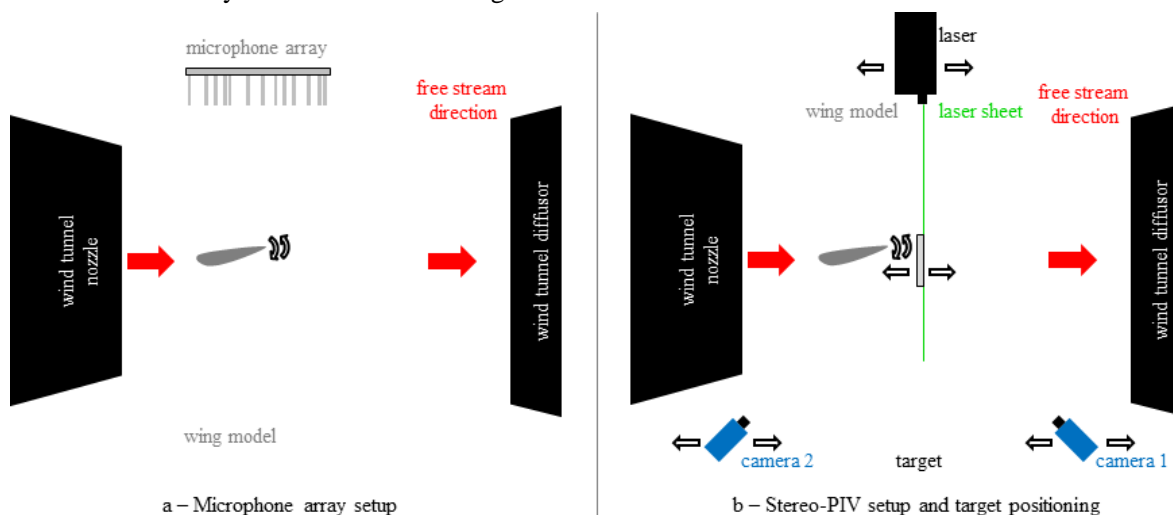


Figure 3 – Schematic drawings of experimental setups in the wind tunnel.

In order to allow for displacement of the region of interest in free stream direction, laser, optics, cameras, mirror, and target mounting are mounted onto traversable systems. Areas under investigation are at quarter chord upstream of the trailing edge, at the trailing edge, and one chord downstream of the trailing edge.

The final setup of the stereoscopic PIV equipment installed around the wind tunnel test section can be seen in Figure 4. Please note that the flow passes from right to left in this view. A boundary layer suction system is used to assure that the development of the boundary layer on the surface of the support structure does not exceed the spacing of the split plate.

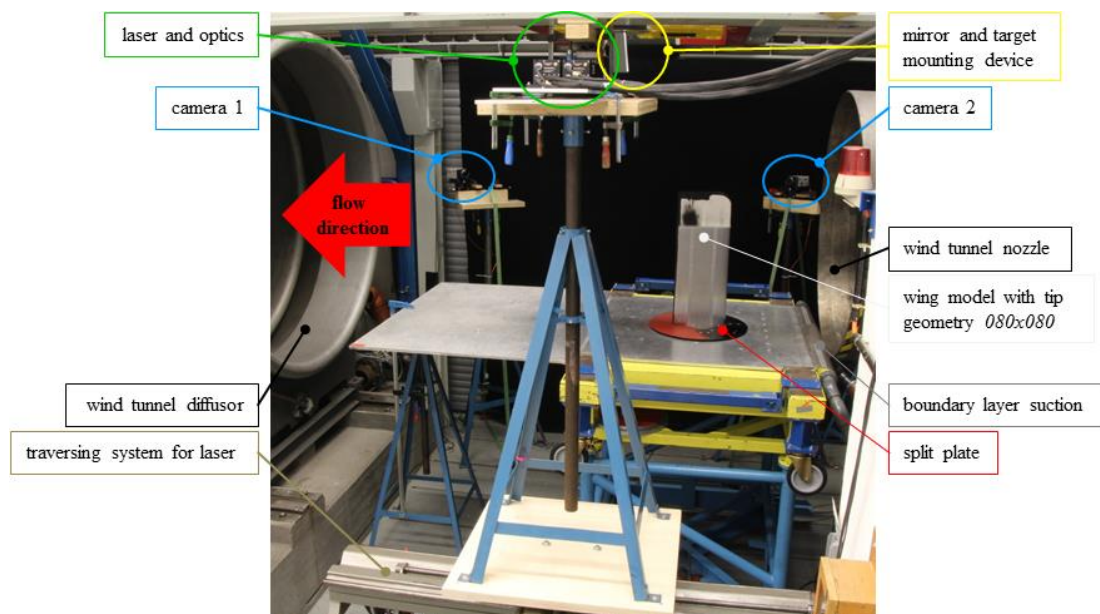


Figure 4 – Experimental setup of stereoscopic PIV system in the wind tunnel of ILR.

4. DATA ACQUISITION AND EVALUATION

Flow field data is acquired at Reynolds number $Re_c = 1,200,000$ based on the chord length, corresponding to a freestream velocities of around $U_\infty = 60$ m/s. Furthermore, the angle of attack is varied from a low setting of $\alpha = 4^\circ$ to a higher deflection of 7° and a rather large deflection of 10° for each of the Reynolds numbers and measurement planes mentioned above. Thus, a total of 18 measurement series was recorded for every wing tip, each consisting of 500 double frame pictures per camera. Separation time between the two frames is calculated by measuring the laser sheet thickness and freestream velocity and taking into account limitations on the number of particles leaving the region of interest.

Calibration is carried out by *DaVis* software using a third order polynomial approach (12) which leads to a very small calibration error of 0.2 to 0.3 pixels. To minimize potential errors due to a displacement of the calibration plane in comparison to the laser plan, disparity vectors are calculated using the self-calibration mode, relying on the assumption that images recorded at the same time will contain equal information. Further information on errors in the adjustment can be found in Coudert and Schon (6) or Louhichi et al. (10).

As for the acoustic measurements, data is acquired in addition at a Reynolds number of 1,000,000, corresponding to a freestream velocity of about $U_\infty = 50$ m/s. The angle of attack is set to 4° , 7° and 10° for all Reynolds numbers, leading to a total of 27 measurement series. Measurements are performed at a sampling rate of 48 kHz, taking an overall number of 2^{22} samples within a time of almost 90 s. An in-house program based on a simple delay and sum beamforming algorithm is used for the analysis of the acoustic data.

5. RESULTS AND DISCUSSION

Results from PIV experiments will be shown, followed by the analysis of acoustic measurements.

5.1 Flow field analyses and vortex characterization

As expected, different wing tip shapes lead to variations in the vortex structure. This can be seen in Figure 5, where normalized tangential velocity V_t is shown over the distance from the vortex center normalized by the halfspan for comparability of all three of the analyzed wing tip geometries. The velocity profiles are shown for the measurements taken at $Re_c = 1,200,000$ in the furthest downstream area, which is positioned one chord length downstream of the model's trailing edge perpendicular to freestream direction. Gradients of the tangential velocity in the vicinity of the vortex center are steeper for an angle of attack of 4° (Figure 5, left) than for the higher angle of 10° (Figure 5, right) and in both cases are steepest for tip model *080x080*.

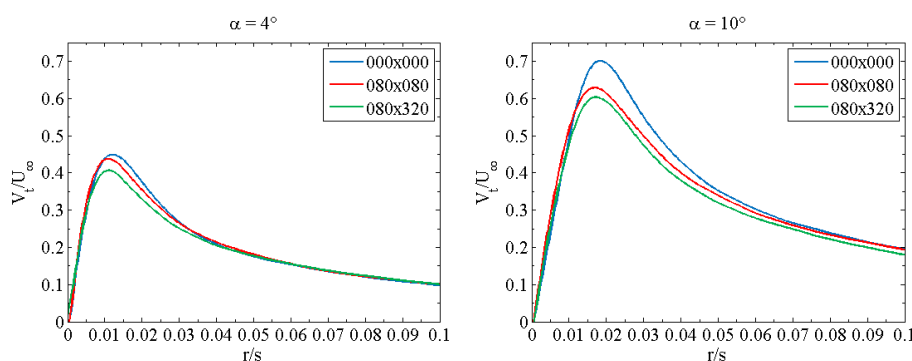


Figure 5 – Normalized tangential velocity V_t at $Re = 1,200,000$ for different tip models at $\alpha = 4^\circ$ and $\alpha = 10^\circ$.

The maximum tangential velocity component along the radius varies by up to 14 percent for the different model geometries in the case of $\alpha = 10^\circ$, where wing tip *000x000* deviates noticeable from the others, showing higher values and a larger spatial expansion than geometries *080x080* and *080x320*. Core sizes of the vortices of the other geometries do not differ significantly, although values of the latter are slightly higher for both deflections.

Vortex structures are further analyzed to investigate the influence of angle of attack on the normalized axial vorticity, as can be seen in Figure 6 showing the most downstream measurement

plane on an equal color range for all subfigures. It applies to all three geometries that for the smaller angle of attack the axial vorticity is more concentrated in the vortex core, while for a larger deflection the core region extends to a larger area and the maximum axial vorticity becomes weaker. This applies to all three wing tip shapes. A trajectory inclination correction has been performed in order to avoid evaluation of the vortex under a deflected angle since the measurement plane is set up perpendicular to freestream velocity and not to the vortex axis. A non-perpendicular cut will lead to a shift between axial and tangential velocities in the vortex and hence to an elongation of the vortex center forming a slightly elliptical shape rather than a circular core area in the distorted image.

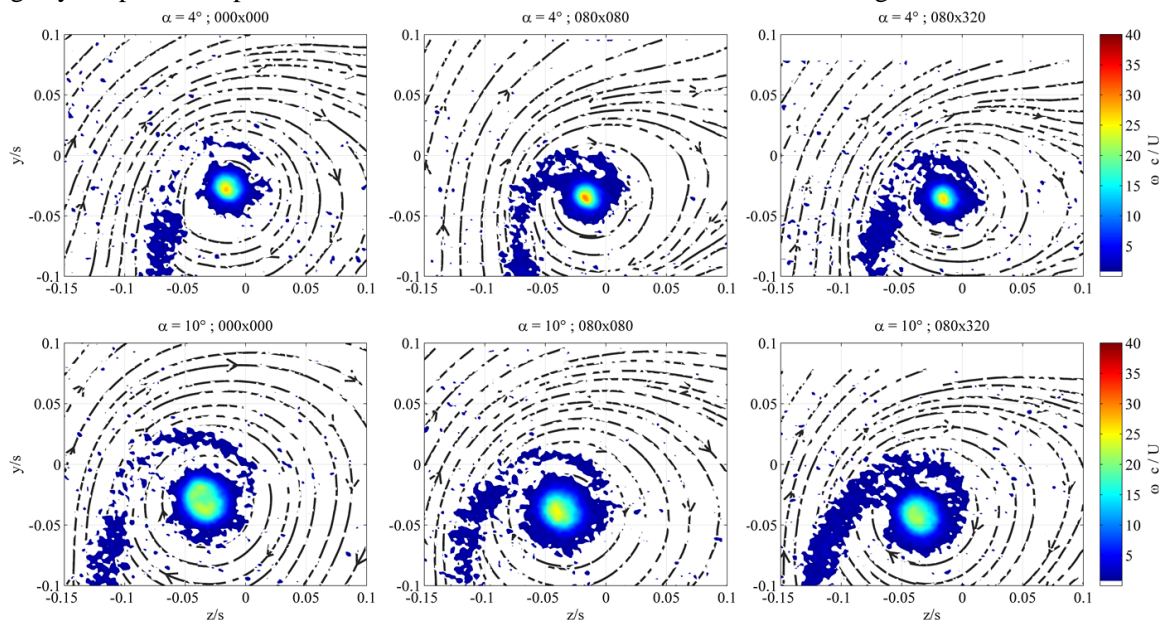


Figure 6 – Normalized axial vorticity at one chord downstream of trailing edge for varying angle of attack.

Analyzing the vorticity plots, the shear layer influence on the flow field is clearly visible as a tail area with higher rotation even one at chord length downstream of the trailing edge. The distance between the vortex core and the shear layer seems not to be affected by the wing tip shape but increases with growing angular deflection. The amount of axial vorticity in the shear layer differs with shape, showing lowest values for the reference case and highest for tip geometry 080x320. The normalized circulation shown in Figure 7 for angles of attack of 4° and 10°, calculated using azimuthal averaging, shows differences in the gradients of different tip shapes. Less concentrated axial vorticity in the core region results in a lower gradient. The analysis leads to the conclusion that for less concentrated vortices vorticity from the shear layer is collected outside of the vortex core region, leading to an increasing amount of circulation. This is for example the case for model 080x320 at $\alpha = 10^\circ$.

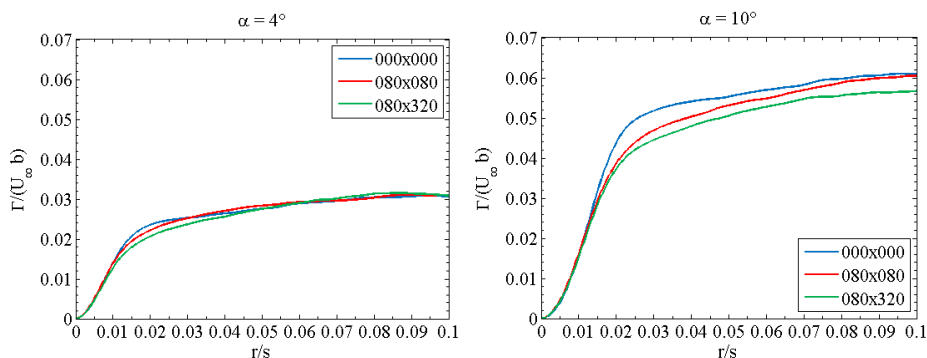


Figure 7 – Normalized circulation at one chord downstream of trailing edge for varying angle of attack.

Figure 8 illustrates axial vorticity in the measurement plane at the trailing edge of the model ($x/c = 0$) for a Reynolds number of 1,200,000. Data from all three geometries is shown with equal color bar settings for comparison, each at angular deflections of 10°.

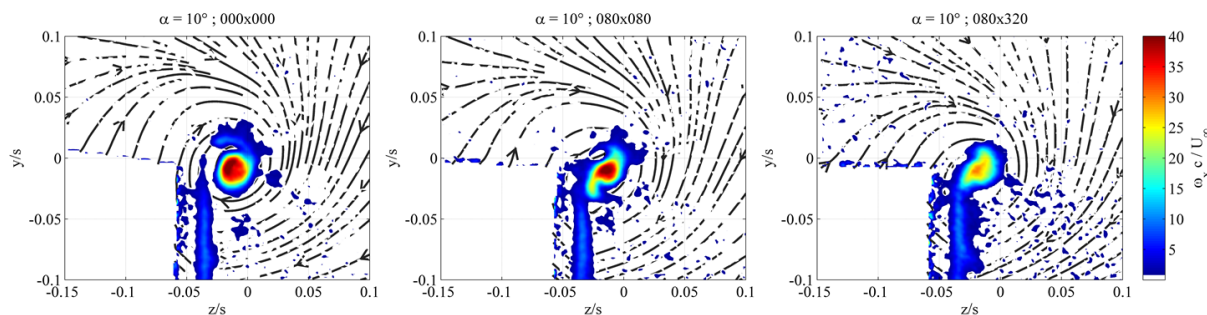


Figure 8 – Axial vorticity for three wing tip shapes at the trailing edge for $\alpha = 10^\circ$.

Tip geometries *080x080* and *080x320* again behave similar, while the coiling process of the reference model is different. The position of the vortex compared to the shear layer visualizes this already: Whereas for the rounded models the vortex center is close to the shear layer, the coiling process clearly shows a spiral shape in the reference case, where the curled shear layer extends significantly outward of the side edge. From the first impression, it can be assumed that the blurred vortex shape of model geometry *080x320* is caused by high fluctuations of the vortex center position during acquisition time. Therefore, the occurrence of the axial vortex center position is plotted over radius in Figure 9. Occurrences spread out more with increasing distance to the trailing edge, but lay within the radius of the vortex core for both cases. Standard deviation, listed in Table 1, confirm that fluctuation is higher in spanwise direction than in z -direction (height of the vortex over suction side of the wing) with only one exemption. This fluctuation may lead to higher noise levels as will be discussed later.

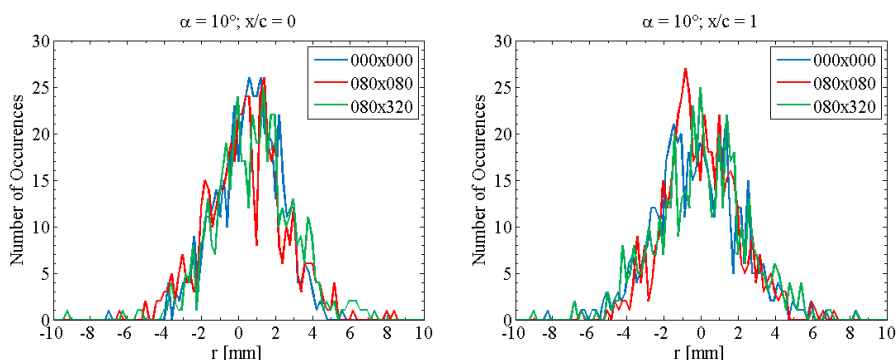


Figure 9 – Occurrence of vortex positions for $\alpha = 10^\circ$.

	$\alpha = 10^\circ; x/c = 0$			$\alpha = 10^\circ; x/c = 1$		
tip geometry	y_{std} [mm]	z_{std} [mm]	σ [mm]	y_{std} [mm]	z_{std} [mm]	σ [mm]
<i>000x000</i>	2,2107	1,4679	2,6537	2,6292	2,1907	3,4222
<i>080x080</i>	1,8595	1,7867	2,5788	2,4770	4,1254	4,8119
<i>080x320</i>	2,2344	1,9165	2,9437	2,4944	2,2647	3,3691

Table 1 – Standard deviation of vortex positions at $\alpha = 10^\circ$ for two measurement planes.

5.2 Microphone spectra and source localization

By evaluating data from the microphone array described above, microphone spectra as well as sound source localization can be calculated. Averaged microphone spectra of the 32 microphones used are shown in Figure 10 for $Re = 1,200,000$ (top) and $Re = 1,000,000$ (bottom) at an angle of attack of 10° over Strouhal number based on the maximum thickness of the model. From frequency spectra (not shown here) it is clearly visible that the peak frequency increases with increasing Reynolds number,

hence with higher velocity. Normalization by freestream velocity and the maximum thickness of the model lead to a Strouhal number of about 10.5.

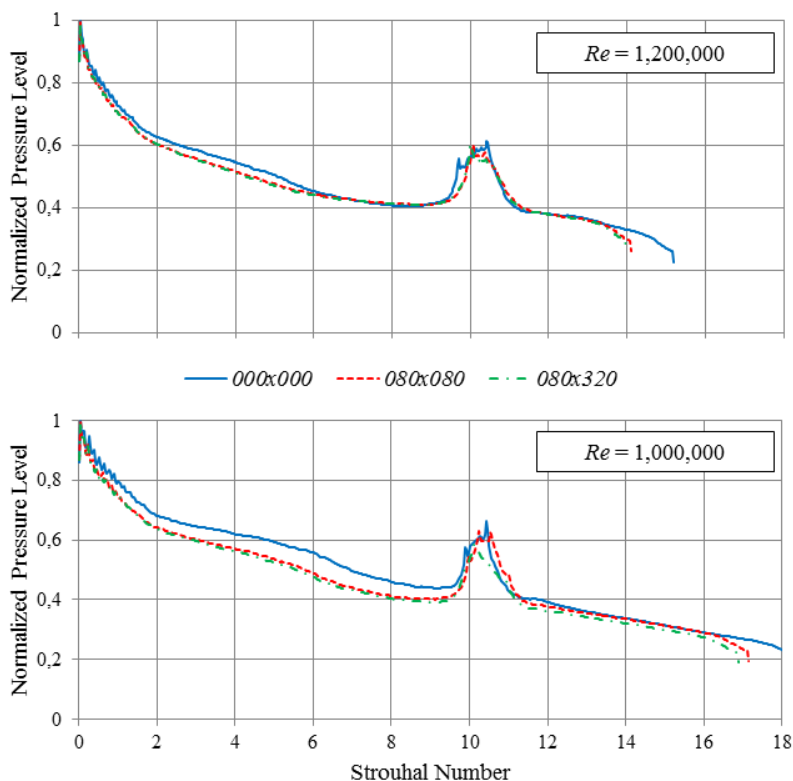


Figure 10 – Normalized pressure levels at different Reynolds numbers for $\alpha = 10^\circ$.

Spectral characteristics illustrate that tip *000x000* varies from both of the other geometries while the latter show similar effects. Peak pressure levels are slightly higher for the reference geometry than for those with rounded or elliptical tip region at the leading edge. A first correlation between flow field and acoustic measurements can be found by comparing the microphone spectra to the tangential velocity distribution (see Figure 5): In both cases, the behavior of the reference model *000x000* differs substantially from those of the rounded shaped geometries. Hence, a correlation between the emerging frequency and the tangential velocity and diameter of the vortex core is assumed.

This phenomenon is investigated more closely in the frequency spectra with regard to the influences of angle of attack and wing tip shape, as shown in Figure 11, again for the Reynolds numbers 1,200,000 and 1,000,000. As described above, the wing tip geometries *080x080* (Figure 11, center) and *080x320* (Figure 11, right) show a similar behavior, particularly the peak shifts from a lower frequency at $\alpha = 4^\circ$ to a higher one for 7° and 10° . On the contrary, in the case of model shape *000x000*, peak frequency decreases with increasing angle of attack (Figure 11, left). In literature, no description of such phenomena could be found yet. The effect might be caused by different noise development processes, e.g. by a switch between wing tip and trailing edge noise. Further investigation is needed for a closer analysis.

Although no correlation can be found depicting the width of the frequency peak with respect to the angle of attack or model geometry in those spectra, the amplitude of the peak is highest in the case of $\alpha = 4^\circ$ for most wing tips and velocities, sole exception being at $Re = 1,000,000$ for model *000x000*. This differs from expectations since a larger angle of attack with higher circulation was expected to cause higher noise levels. Furthermore, peaks for lower angles of attack show a distinct single maximum, while for larger deflections the peak becomes broader with several local maxima. This compares well with the size of the vortex core which increases with higher deflection angles. Therefore, a correlation may be found in assuming that a concentration of vorticity in the vortex center may lead to a slender peak in the frequency spectrum.

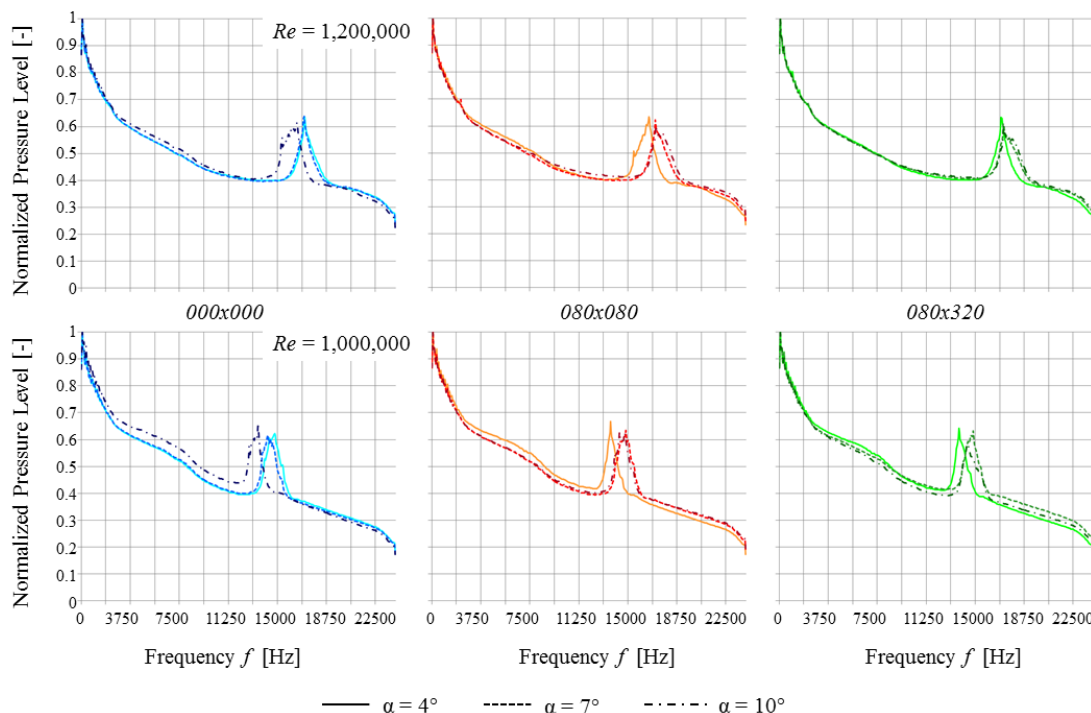


Figure 11 – Microphone spectra for different Reynolds numbers and angles of attack by wing tip geometry.

Last, Figure 12 shows the sound source localization calculated via beamforming algorithm for two wing tip geometries according to their peak frequencies from the microphone spectra. The shift of the noise source in *y*-direction is due to the varying halfspan of the wing models while using the same setup of the microphone array. Although no deconvolution has been applied, the primary lobe of the noise source is clearly visible at the wing tip trailing edge. Through utilization of methods such as Damas, spatial correlation or point spread functions, the source will become even more distinct since secondary lobes will be diminished.

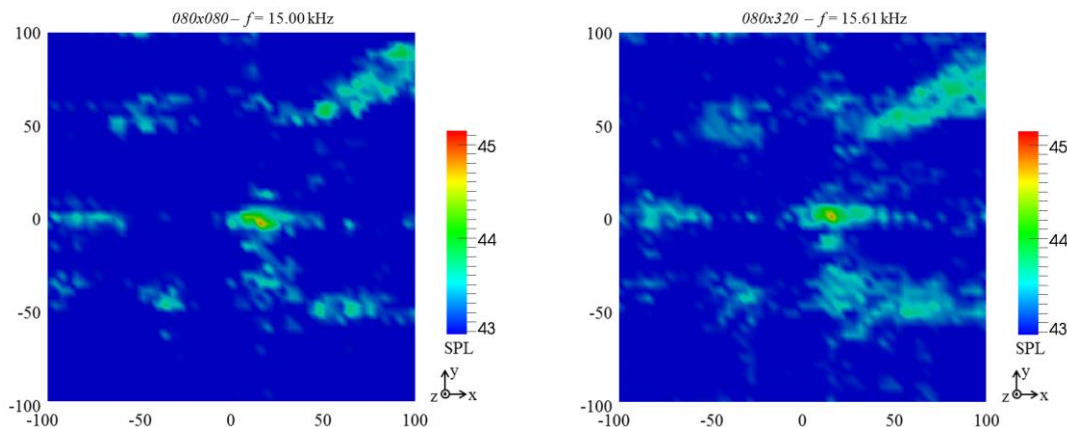


Figure 12 – Noise source localization for two different wing tips at $Re = 1,200,000$.

By calculating the microphone spectra with a Strouhal number based on the trailing edge thickness, t_{TE} , the peak occurs at $St = 0,21$ for both cases from Figure 10. This indicates, in combination with the noise maps above, that the noise radiates from the trailing edge corner of the wing. Therefore, it will be influenced by the fluctuation of the vortex center position as shown in Figure 9.

6. CONCLUSIONS AND OUTLOOK

From the first analyses of measurement data and comparison, the elliptical variation of the leading edge tip region clearly shows an influence not only in the flow field parameters and vortex

characteristics, as was stated by Buffo et al. (4), but moreover also effects the noise generation and development. From PIV and acoustic measurements, influences were shown which illustrate the correlation between the vortex structure and the frequency spectrum characteristics. The amounts of tangential velocity components and axial vorticity as well as the size of the vortex core seem to be important parameters to influence the generation of noise. To go into more detail on the produced sound levels, deconvolution and filtering to achieve a diminution of secondary lobes in the beamforming results will be performed. Analyses of different Reynolds numbers will provide more detailed insights into the developing vortex structure, expecting the axial vorticity to increase with higher Reynolds numbers and the vortex core region to become more intensive and more concentrated because of stronger velocity gradients.

However, the most striking aspect is the dependency of frequency shifting on the wing tip shape. This effect may be caused by different noise generation processes based on varying coiling processes of the shear layer. Because of this effect, shaping of the wing tip region shows a great potential in frequency modulation and thus in the possibility of decreasing noise annoyance. This effect is especially interesting in the vicinity of airports as different tonal frequencies, although at equal sound level, are perceived at dissimilar levels of annoyance.

Taking this as basis, the influence of elliptical shaping in particular and of the interaction of vortex characteristics and noise development in general can be analyzed. The detailed analysis of the flow field will severely contribute to the understanding of noise generation since many effects are not yet clearly developed in literature. Especially unsteady phenomena will affect noise generation.

REFERENCES

1. Arbey H, Bataille J. Noise generated by airfoil profiles placed in a uniform laminar flow. *J Fluid Mech.* 1983;134:33-47.
2. Arcondoulis EJG, Doolan CJ, Zander AC. Airfoil noise measurements at various angles of attack and low Reynolds number. *Proc Acoustics 2009: 23-25 November 2009; Adelaide, Australia 2009.*
3. Brooks TF, Marcolini MA. Airfoil tip vortex formation noise. *AIAA J.* 1986;24(2):246-52.
4. Buffo RM, Wolf CC, Dufhaus S, Hoernschemeyer R, Stumpf E. Vortex creation and wing-tip geometry dependencies. *Proc 30th AIAA Applied Aerodynamics: 25-28 June 2012; New Orleans, USA 2012.*
5. Chong TP, Joseph P. An experimental study of tonal noise mechanism of laminar airfoils. *Proc 15th AIAA/CEAS Aeroacoustics (30th AIAA Aeroacoustics): 11-13 May 2009; Miami, USA 2009.*
6. Coudert SJM, Schon JP. Back-projection algorithm with misalignment corrections for 2D3C stereoscopic PIV. *Meas Sci Technol.* 2001;12:1371-81.
7. Hamakawa H, Hosokai K, Adachi T, Kurihara E. Aerodynamic sound radiated from two-dimensional airfoil with local porous material. *Open J Fluid Dyn.* 2013;3:55-60.
8. Henning A, Kaepernick K, Ehrenfried K, Koop L, Dillmann A. Investigation of aeroacoustic noise generation by simultaneous particle image velocimetry and microphone measurements. *Exp Fluids* 2008;45(6):1073-85.
9. Liu Z, Zheng Y, Jia L, Jiao J, Zhang Q. Stereoscopic PIV studies on the swirling flow structure in a gas cyclone. *Chem Eng Sci.* 2006;61:4252-61.
10. Louhichi H, Fournel T, Lavest JM, Ben Aissia H. Self-calibration of Scheimpflug cameras: An easy protocol. *Meas Sci Technol.* 2007;18:2616-22.
11. Paterson RW, Vogt PG, Fink MR, Munch, CL. Vortex noise of isolated airfoils. *J Aircraft.* 1973;10(5):296-302.
12. Raffel M, Willert CE, Wereley ST, Kompenhans J, *Particle Image Velocimetry – A practical guide.* 2nd ed. Berlin, Germany: Springer; 2007.
13. Storms BL, Hayes JA, Jaeger SM, Soderman PT. Aeroacoustic study of flap-tip noise reduction using continuous moldline technology. *Proc 6th AIAA/CEAS Aeroacoustics (21st AIAA Aeroacoustics); 12-14 June 2000; Lahaina, USA 2000.*
14. Thota NM, Brooks LA, Moreau DJ, Zander AC, Doolan CJ. Analysis of noise generated by a wall mounted finite-length airfoil. *Proc Acoustics 2011; 2-4 November 2011; Gold Coast, Australia 2011.*
15. Tiedemann C, Neuwerth G, Henke R. Localisation of flap edge sound sources by use of spectral analysis and flow investigation. *Proc 12th AIAA/CEAS Aeroacoustics (27th AIAA Aeroacoustics): 8-10 May 2006; Cambridge, USA 2006.*